Functionalized Fe-Filled Multiwalled Carbon Nanotubes as Multifunctional Scaffolds for Magnetization of Cancer Cells

*Riccardo Marega, Federica De Leo, Florent Pineux, Jacopo Sgrignani, Alessandra Magistrato, Anil Damodar Naik, Yann Garcia, Lionel Flamant, Carine Michiels, and Davide Bonifazi**

Dedicated to Professor Alain Krief on the occasion of his 70th birthday

With the aim to design addressable magnetically-active carbon nanotubes (CNTs) for cancer treatment, the use of Fe-filled CNTs (Fe@MWCNTs) as multifunctional scaffolds is reported for exohedrally anchoring a monoclonal antibody (mAb) known to bind a plasma membrane receptor over-expressed in several cancer cells (EGFR). Comprehensive microscopic (transmission electron microscopy, atomic force microscopy, and scanning electron microscopy) and spectroscopic (Raman, ^{57}Fe Mossbauer, energy dispersive spectroscopy, X-ray photoelectron spectroscopy (XPS), X-ray diffraction) characterizations reveal the efficient confinement of magnetically-active Fe phases (α-Fe and Fe_3C), while compositional evaluations through XPS, thermogravimetric analysis and gel electrophoresis confirm that mAb immobilization onto Fe@MWCNTs occurs. Enzyme-linked immunosorbent assay (ELISA), confocal microscopy imaging and western blotting confirm the targeting action toward EGFR-overexpressing cell lines (EGFR+). In vitro magnetic filtration experiments demonstrate that a selective removal of EGFR+ cells from a mixed population of healthy cell lines could be obtained in very short times (≈10 min). Cytotoxicity evaluations by classic cell staining procedures after application of an electromagnetic radiation inducing magnetic fluid hyperthermia (MFH), show a selective suppression of the EGFR+ cell line. Molecular dynamics and docking simulations of the hybrid mAb/Fe@MWCNTs conjugates nicely show how the presence of the CNT framework does not sterically affect the conformational properties of the two antigen binding regions, further supporting the biochemical findings.

1. Introduction

With over 10 million new cases per year worldwide, cancer remains one of the challenging class disease to treat and a significant cause of morbidity and mortality.[1] It is thus of paramount importance to rapidly develop multifunctional theranostic technologies able to simultaneously detect and selectively eradicate both primary tumors and metastasis, the latter being the major causes of death. In this respect, CNT derivatives, with their graphitic shells and long tubular structures,[2] have recently been proposed as alternative multifunctional nanostructures in nanomedicine for imaging,[3] tissue engineering,[4] drug-delivery[5] and qs anticancer platforms.[6] Numerous in vitro and in vivo studies have been reported toward the understanding of CNTs biological properties.[7] Specifically, it has been experimentally demonstrated that CNTs can efficiently target cancer cells in vivo[7j,8] and allow non-invasive (e.g., light-[9] or radiofrequency-field induced[10]) hyperthermal treatment or in situ delivery of anticancer drugs for suppressing

Dr. R. Marega, F. De Leo, F. Pineux, Prof. D. Bonifazi
Department of Chemistry and Namur
Research College (NARC),
University of Namur
Rue de Bruxelles 61, Namur, 5000, Belgium
E-mail: davide.bonifazi@fundp.ac.be
Dr. D. Bonifazi
Department of Pharmaceutical and Chemical Science
and INSTM UdR Trieste
University of Trieste
Piazzale Europa 1, Trieste, 34127, Italy
Dr. J. Sgrignani, Dr. A. Magistrato
CNR-IOM-DEMOCRITOS National Simulation Center at SISSA
International School for Advanced Studies (SISSA/ISAS)
via Bonomea 265, Trieste, 34151, Italy
Dr. A. D. Naik, Prof. Y. Garcia
Institute of Condensed Matter and Nanosciences
MOST–Inorganic Chemistry
Université Catholique de Louvain
Place L. Pasteur 1, Louvain-la-Neuve, 1348, Belgium
L. Flamant, Prof. C. Michiels
Unité de Recherche en Biologie
Cellulaire (URBC) and NARILIS
University of Namur
Rue de Bruxelles 61, Namur, 5000, Belgium

DOI: 10.1002/adfm.201202898

malignant cells. Additionally, it turned out that while long (>5 μm) pristine CNTs can induce cytotoxicity and inflammatory responses if inhalated,[11] intravenous or intratumor administration of short (<500 nm) or exohedrally functionalized CNTs[12] equipped with bioactive molecules,[7f,13] revealed to be non toxic[14] and were found to be expelled in urine[15] and fecal excretions.[16] Apart from the exosurface, CNTs possess an inner empty tubular phase into which a large variety of functional guests can be incorporated through two circular clefts located at the extremities[17] with the graphitic layers acting as suitable shells shielding the inner guests from the external environment and allowing further chemical processability.[18] Due to the variety of diameters (from 1 nm to 40–50 nm depending on the CNT structure), such cavities can be used to selectively confine, recognize, or isolate a large series of functional organic (C_{60} or its derivatives,[19] pentacene, anthracene, tetrathiafulvalene, and tetracyano-*p*-quinodimethane)[20] and inorganic (Sn microcrystals displaying super-conducting properties,[21] nanoparticles,[22] lanthanide inorganic salts $LnCl_3$[23] and Gd, Cu, and Ni[24]) or bioactive guests.[25] Moreover, as many significant chemical transformations have been achieved to selectively functionalize CNT's wall,[12,26] this structure can be easily modified to make these compounds more dispersable in aqueous media, and thus of potential use in biomedical applications.[7i] Among the different encapsulable bioactive nanomaterials,[27] magnetic nanoparticles (MNPs)[28] are clear potential candidates for biomedical applications,[29] such as for selective filtration/separation of biological species,[30] magnetic drug-targeting and/or delivery (MDT and MDD respectively)[31] magnetic resonance imaging (MRI),[31a,32] and localized magnetic fluid hyperthermia (MFH)-based treatments.[33] Recently, some examples of exohedral MNPs-CNT nanohybrids have been reported for MDT chemotherapy[34] or bioimaging purposes,[35] while weakly-magnetic CNTs, encapsulating minor catalyst residues,[36] have been tested for shuttling genetic material inside cells,[37] for MDT,[38] and for specific protein binding,[30i] respectively. Biocompatibility studies of metal-filled CNTs (M@CNTs)[39] in the presence of lipids[40] or human serum albumin[41] and high drug-loading capacity[42] have been also reported. Recently, Fe-filled multiwalled CNTs (Fe@MWCNTs), noncovalently functionalized with pluronic F127 were developed for in vitro MR-guided laser-induced thermotherapy, with promising outcomes.[9] Although the loading (3 wt%) of the encapsulated Fe revealed to be enough for the MRI application, it is certainly too low for eliciting magnetically-induced curative responses. With the aim to design addressable magnetically-active CNTs for cancer treatment, in this work we propose to use Fe@MWCNTs as multifunctional scaffolds for exohedrally anchoring a monoclonal antibody (mAb) targeting cancer cells and endohedrally confining Fe-based magnetic phases. mAb *Cetuximab*,[43] known to selectively bind the epidermal growth factor receptor (EGFR,[44] a plasma membrane receptor over-expressed in several cancer cells),[45] has been selected as the targeting unit. Comprehensive microscopic (transmission electron microscopy (TEM), atomic force microscopy (AFM), and scanning electron microscopy (SEM)) and spectroscopic (Raman, ^{57}Fe Mossbauer, energy dispersive spectroscopy (EDS), X-ray photoelectron spectroscopy (XPS), and X-ray diffraction (XRD)) characterizations displayed the efficient confinement of magnetically-active Fe phases (α-Fe and Fe_3C) inside MWCNTs, while classical compositional evaluations through XPS, thermogravimetric analysis (TGA) and gel electrophoresis confirm the occurred mAb immobilization onto Fe@MWCNTs. In vitro magnetic filtration experiments demonstrate that a selective removal of cancer cells from a mixed population of healthy cell lines could be obtained with mAb-bearing Fe@MWCNTs in very short times (~10 min). Cytotoxicity assessments underline a good biocompatibility profile of the carbon hybrids towards the chosen cell lines. Preliminary MFH experiments in the presence of the nanobioconjugates showed a high selectivity toward the suppression of cancer cells.

2. Results and Discussion

2.1. Synthesis of Fe@MWCNTs

By using a ferrocene-catalyzed chemical vapor deposition (CVD) process with toluene as complementary sourcing carbon feedstock, Fe-filled MWCNTs (Fe@MWCNTs) have been batchwise produced inside a furnace kept at 1123 K under Ar atmosphere, (reaction time = 15 min, schematization and details in Supporting Information Figure S1). Detailed microscopy-based characterizations such as bright-field TEM (**Figure 1**a and Supporting Information Figure S2), tapping-mode AFM

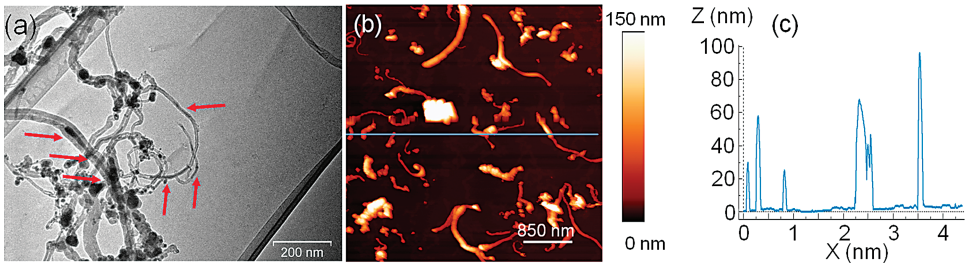

Figure 1. Microscopic characterization of **Fe@MWCNTs** as deposited from a dispersion (0.1 mg mL^{-1}) in dimethylformamide (DMF). a) Representative TEM image after deposition on carbon-coated Cu grid, displaying the presence of the encapsulated Fe (see arrows). b) Tapping-mode AFM images of a mica surface spin-coated with the DMF dispersion, showing isolated tubular structures with c) height cross-sections ranging from 20 to 100 nm (in other samples, not displayed here, CNTs with diameters at around 10 nm have been also observed).

Table 1. Compositional data of **Fe@MWCNT**s as evaluated by EDS and XPS.

Element	EDS [wt%]	EDS [at%]	XPS [at%]
C	83.56 ± 3.01	92.62 ± 1.09	93.69 ± 3.11
O	5.81 ± 1.53	4.82 ± 1.20	6.31 ± 3.11
Fe	10.60 ± 3.68	2.55 ± 0.97	

(Figure 1b,c and Supporting Information Figure S3), and SEM (Supporting Information Figure S4) revealed the presence of twisted, very thick MWCNTs with outer diameters ranging from 10 to 100 nm and lengths in the order of 0.5–5 μm, the latter being a direct consequence of the very short reaction time. In particular, the TEM investigations showed the presence of CNTs occasionally filled with a highly electron-blocking material, suggesting the presence of metallic (Fe) phases. Raman spectroscopy analysis of Fe@MWCNTs (λ_{exc} = 633 nm) supports the structural evidences as obtained by the microscopic investigations, since the typical signatures for MWCNTs are present at 1583 cm^{-1} and 1329 cm^{-1} for the sp^2-(graphitic) and sp^3-hybridized (defect sites) C atoms, respectively (Supporting Information Figure S5).

To determine the presence of the encapsulated Fe phases in the Fe@MWCNTs samples, X-ray characterizations were carried out as first tool. The compositional data (weight and atomic percentages, wt% and at%, respectively) obtained by EDS (z-scanning depth ~600 nm, according to Castaing's formula,[46] Supporting Information Figure S6) and XPS (z-scanning depth ~3–12 nm,[47] Supporting Information Figure S7) revealed the presence of peaks attributed to carbon (C Kα_1 at 0.277 KeV by EDS, C 1s at 284.5 eV by XPS) and oxygen (O Kα_1 at 0.525 KeV by EDS, O 1s at 533 eV by XPS, **Table 1**). Intense Fe signals were only apparent in the EDS spectra (FeKα_1 at 6.398 KeV), suggesting effective Fe localization in the deeper layers of Fe@MWCNTs.

Interestingly, the Fe amount as revealed by EDS (10.60 wt%, 1.9 μmol mg^{-1}) was confirmed by TGA under air atmosphere, as the complete carbon pyrolysis leaded to quantifiable residues of iron oxides (25.17 wt%, 1.6 μmol mg^{-1}, Supporting Information 8). ^{57}Fe Mössbauer spectroscopy was also used to both identify and quantify the different iron species. The spectrum at 298 K (**Figure 2**a) is a superposition of an intense singlet and two magnetically split sextets, corresponding to γ-Fe, α-Fe and Fe_3C phases, respectively. Spectra recorded in a larger velocities range (±12 mm s^{-1}) did not reveal any additional components, thus unambiguously excluding the presence of iron oxides and supporting our evidences that all iron phases are encapsulated inside the nanotube framework. At 77 K, both hyperfine magnetic fields of α-Fe (B_{hf} = 33.8 T) and Fe_3C (B_{hf} = 24.8 T) increased as expected.[48] The increase in linewidth of the singlet ($\Gamma/2$ = 0.33(2) mm s^{-1}) is presumably due to the onset of an antiferromagnetic ordering for γ-Fe particles.[49] Assuming that all species have the same probability of recoil-free emission at a given temperature and the area fraction of the two sextets remains roughly the same at both temperatures, except for a small increase in the area of γ-Fe, the ratio of 1/1.5/0.5 for γ-Fe, Fe_3C and α-Fe phases, respectively (Supporting Information Table S1), was determined. The presence of α-Fe, γ-Fe and Fe_3C phases have been further confirmed by X-ray diffraction (XRD) analysis (Figure 2b). Comparing the experimental data (Figure 2b) with those from the JCPDS-ICDD database (no. 06-0696 for α-Fe; 35-0772 for Fe_3C; see ref.[50] for γ-Fe), one can clearly confirm the presence of magnetic Fe phases such as α-Fe (at 44.71 and 65.09 deg) and Fe carbides (at 37.72, 54.25, 70.85, and 82.23 deg) in addition to the graphitic-centered signals at 26.02 deg. (Supporting Information Figure S9).

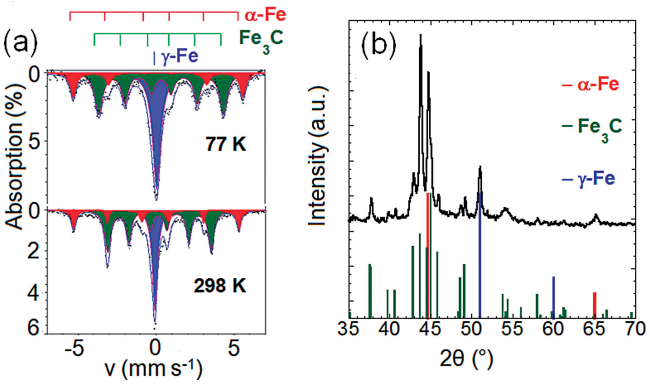

Figure 2. a) ^{57}Fe Mössbauer spectra: the singlet with isomer shift, δ = 0.09(3) mm s^{-1} and line width $\Gamma/2$ = 0.2(2) mm s^{-1} is assigned to paramagnetic γ-Fe.[51] At 298 K, the sextet-1 with δ = 0.19(5) mm s^{-1}, quadrupole shift ε = 0.02(5) mm s^{-1} and hyperfine magnetic field (B_{hf}) of 20.6 T corresponds to Fe_3C, whereas sextet-2 (lowest relative contribution) with zero isomer and quadrupole shifts indicates a cubic symmetry (B_{hf} = 33.1 T), typical for ferromagnetic α-Fe.[50] (b) XRD pattern for a **Fe@MWCNTs** sample.

2.2. Organic Functionalization of Fe@MWCNTs

Exohedral functionalization of **Fe@MWCNTs** was achieved upon addition reaction to CNTs by mixing a Boc-proteced aniline derivative (*tert*-butyl 4-aminobenzylcarbamate, **Figure 3**) with isoamyl nitrite, following a slight modification of the procedure reported by Tour and co-workers.[52] Resulting **Fe@MWCNTs-NH-Boc** carbon nanotubes were then Boc-deprotected with a 4M HCl solution in dioxane,[53] affording conjugate **Fe@MWCNTs-NH_2**, exohedrally exposing free benzylic amino groups. Amidation reaction of **Fe@MWCNTs-NH_2** with mAb in the presence of 1-ethyl-3-(dimethylaminopropyl)carbodiimmide (EDC) under buffer conditions, yielded final bioconjugate **Fe@MWCNTs-NHCO-Ab** (Figure 3). As reference material, non-targeting protein bovine serum albumin (BSA) has been also covalently coupled to **Fe@MWCNTs-NH_2**, yielding water-dispersable **Fe@MWCNTs-NHCO-BSA** nanohybrids (Figure 3). It should be pointed out that the acidic treatment (with HCl) employed in the Boc-cleavage step might cause a dramatic reduction of the metal content, unless properly confined inside the CNTs. However, EDS analysis of the final **Fe@MWCNTs-NHCO-Ab** conjugate revealed a Fe content of 7.16 ± 1.96 wt% (Supporting Information Figure S10), thus displaying a minor loss of Fe with respect to the content as measured for the **Fe@MWCNTs** precursors (the introduction of about 10 wt% of organic moiety

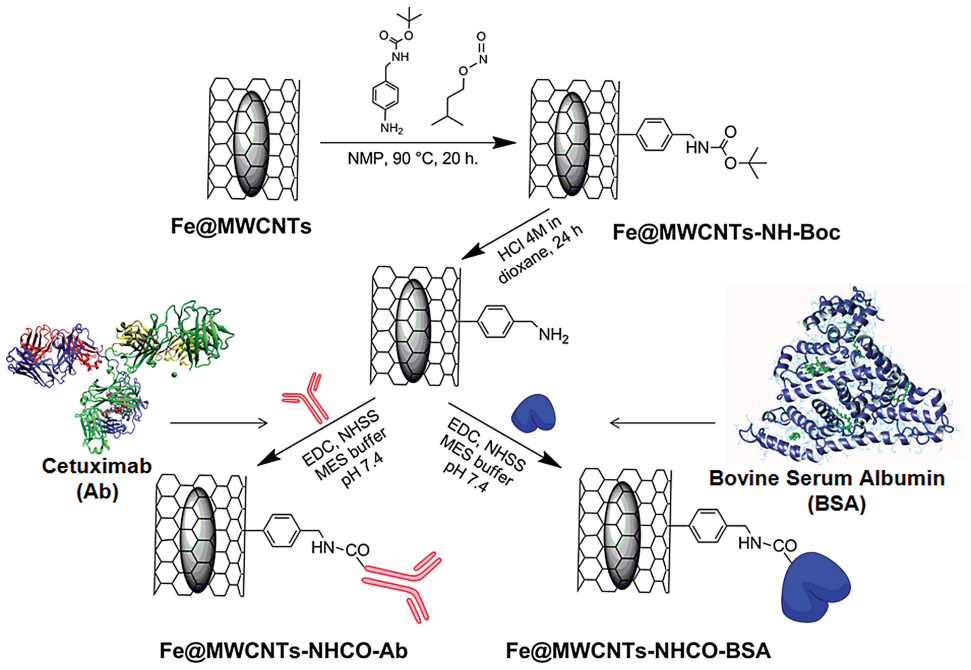

Figure 3. Schematic representation of the synthetic routes towards bioconjugates **Fe@MWCNTs-NHCO-Ab** and **Fe@MWCNTs-NHCO-BSA**.

after organic functionalization and bioconjugation should be also taken in to account). To monitor the organic functionalization of **Fe@MWCNTs**, XPS and TGA characterizations have been also carried out. Whereas a relatively weak signal belonging to the N atoms (N 1s at 400 eV) was detected for the BOC-protected **Fe@MWCNTs-NH-Boc** (0.86 ± 0.29 at%) and free-amino **Fe@MWCNTs-NH_2** (0.80 ± 0.62 at%) derivatives, after protein conjugation both N- and O-centered peaks (O 1s at 533 eV) dramatically increased for **Fe@MWCNTs-NHCO-Ab** and **Fe@MWCNTs-NHCO-BSA** samples, supporting the effective grafting of the protein moiety onto **Fe@MWCNTs-NH_2** (**Table 2**, Supporting Information Figure S11).

TGA plots for both **Fe@MWCNTs-NHCO-Ab** and **Fe@MWCNTs-NHCO-BSA** samples clearly showed the typical protein thermal signature at ~573 K, displaying a biofunctionalization degree of 1.0 and 0.5 nmol mg^{-1}, respectively (Supporting Information Figure S12). Covalent immobilization has been further assessed by gel-electrophoresis (GE) studies[54] of both **Fe@MWCNTs-NHCO-Ab** and **Fe@MWCNTs-NHCO-BSA** in the presence of their respective reference free proteins, namely mAb and BSA (Supporting Information Figure S13). All **Fe@MWCNT** derivatives did not penetrated inside the gel and precipitated in the deposition well, while reference free proteins differently migrated. Notably, no bands belonging to unbounded proteins could be detected in both nanobioconjugate lanes, thus suggesting the effectiveness of the covalent linkage and of the product purification technique.

To further verify the protein covalent grafting on **Fe@MWCNTs**, equivalent physical mixtures (in terms of **Fe@MWCNTs** and antibody contents, as determined by TGA) between **Fe@MWCNTs** and mAb (i.e., **Fe@MWCNTs/Ab**, eventually formed through hydrophobic interactions, see also the modelling section) or **Fe@MWCNTs-NH_2** and mAb (i.e., **Fe@MWCNTs-NH_2/Ab**, eventually formed through both hydrophobic and coulombic interactions), were prepared and analysed by GE (Supporting Information Figure S13). By comparing covalent bioconjugate **Fe@MWCNTs-NHCO-Ab** with both **Fe@MWCNTs/Ab** and **Fe@MWCNTs-NH_2/Ab**, one can clearly see that for **Fe@MWCNTs/Ab** and **Fe@MWCNTs-NH_2/Ab** considerable amounts of non-bounded mAb are present, whereas no traces of the free protein are observed for **Fe@MWCNTs-NHCO-Ab**.

Table 2. Compositional data for the **Fe@MWCNT** derivatives as obtained by XPS (mean ± SD after three different measurements).

Sample	C 1s [284.5 eV]	N 1s [400.0 eV]	O 1s [533.0 eV]
Fe@MWCNTs	93.69 ± 3.11	–	6.31± 3.11
Fe@MWCNTs-NH-Boc	95.59 ± 0.50	0.86 ± 0.29	3.55 ± 0.22
Fe@MWCNTs-NH_2	94.78 ± 0.62	0.80 ± 0.62	4.41 ± 0.63
Fe@MWCNTs-NHCO-Ab	83.15 ± 0.56	6.58 ± 0.28	10.27 ± 0.42
Fe@MWCNTs-NHCO-BSA	86.64 ± 2.67	3.60 ± 0.79	9.75 ± 3.39

2.3. Binding Selectivity Studies

As a first assessment to evaluate the targeting activity of the bio-conjugated MWCNTs derivatives, ELISA tests have been performed to screen the binding selectivity of the mAb alone (**Figure 4**a) and that of **Fe@MWCNTs-NHCO-Ab** towards EGFR-overexpressing (EFGR+) cells (A431) and cell lines that do not overexpress (EFGR-) the receptor (EAhy926 and CHO).

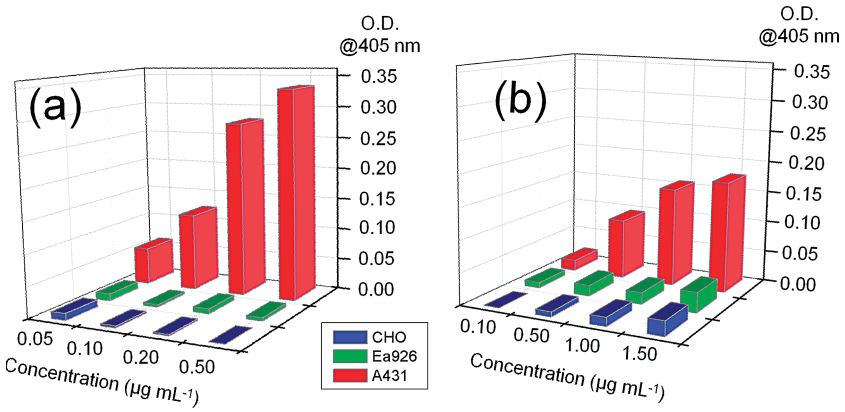

Figure 4. ELISA results on A431, EAhy926 and CHO cells of a) free mAb and b) **Fe@MWCNTs-NHCO-Ab** (concentration expressed in terms of the mAb concentration). See Supporting Information Table S2 for values and standard deviations.

As it clearly appears from the histograms shown in Figure 4b, bioconjugate **Fe@MWCNTs-NHCO-Ab** showed a pronounced concentration-dependent selectivity towards A431 cells and very low nonspecific-binding activity towards EFGR- EAhy926 and CHO cells, thus retaining the original mAb activity and specificity.

To further prove the binding properties of the mAb-CNTs bioconjugate, we have validated the field-induced self-sorting abilities of **Fe@MWCNTs-NHCO-Ab** toward the in vitro recovering of EGFR-overexpressing cells under the application of an external magnetic field (coercive field strength = 900 KA m^{-1}). At first, the conditions to efficiently remove **Fe@MWCNTs-NHCO-Ab** from dispersions in a CO_2-independent medium through magnetic filtration were screened. As imaged by phase-contrast confocal microscopy, 8 min of magnetic filtration resulted to be sufficient for ensuring the complete abstraction of **Fe@MWCNTs** with concentration of 100 μg mL^{-1} in 1.5 mL of medium (Supporting Information Figure S14). Subsequently, different cell lines were stained with red (A431), green (EAhy926) and blue (CHO) emitting dyes and mixed in similar proportion in 1.5-mL-vials containing CO_2-independent medium (about 200 000 cells mL^{-1} each, **Figure 5**a, step I). Nanohybrid **Fe@MWCNTs-NHCO-Ab** or the reference derivatives, **Fe@MWCNTs/Ab** and **Fe@MWCNTs-NHCO-BSA**, were introduced at an equivalent **Fe@MWCNTs** concentration of 100 μg mL^{-1} (step II) and immediately analyzed by confocal microscopy. After 2.5 min under gentle shaking to allow binding to occur (step III) and 8 min of exposure to the magnetic field (step IV), the supernatant was gently withdrawn with a micropipette and analyzed, whereas the magnetically-induced precipitate was re-dispersed in CO_2-independent medium prior to analysis (step V). As a first test, A431, CHO and EAhy926 cells were mixed together and magnetically sorted with **Fe@MWCNTs-NHCO-Ab**, resulting in the isolation of the EGFR+ cells, the former being only observed in the precipitate (Figure 5b(I,IV,VII). The same test was repeated with **Fe@MWCNTs/Ab**. This time a less efficient abstraction of A431 cells from the medium can be clearly observed, most probably caused by the presence in solution of mAb units that deadsorbing from the CNTs surface are ineffective for the magnetic sorting (Figure 5b(II,V,VIII). As expected, no selective removal of any of the three cell lines occurred upon addition of non-specific **Fe@MWCNTs-NHCO-BSA** reference nanoconjugates (Figure 5b(III,VI,IX)). Notably, in any of the studied combinations, no MWCNTs residues have been observed in the supernatant solution after application of the magnetic field. Only a very few number of EGFR- cells were found in the magnetic precipitates (Figure 5b(VII,VIII,IX)), mainly as a consequence of manipulation maneuvers during the removal of the supernatant. It should be pointed out that two min of magnetic filtration were enough to selectively isolate the cancer cells, but ineffective for the complete abstraction of the unbound **Fe@MWCNTs-NHCO-Ab** (Supporting Information

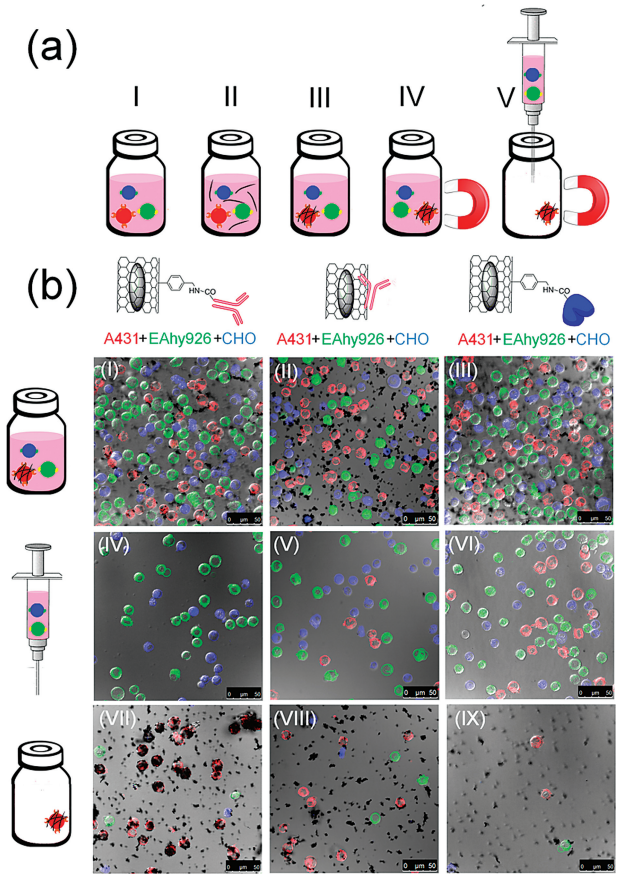

Figure 5. a) Magnetic sorting manipulation steps: (I) mixing of stained cells, (II) addition of the CNT derivatives at an equivalent concentration of 100 μg mL^{-1}, (III) gentle agitation (2.5 min) to allow the binding to occur, (IV) magnetic filtration (8 min) with a permanent magnet with a coercive field strength of 900 KA m^{-1}, and (V) separation between the supernatant and magnetic precipitate with a micropipette. (b) Confocal microscopy images of suspensions containing A431 (red), and EGFR-, CHO (blue) and EAhy926 (green) cells after the magnetic filtration treatments with **Fe@MWCNTs-NHCO-Ab**, (first column), **Fe@MWCNT/Ab** (second column) and **Fe@MWCNTs-NHCO-BSA** (third column). (I–III) Images obtained after mixing the cells and the CNTs bioconjugates at t_0; (IV–VI) supernatants and (VII–IX) magnetically-induced precipitates as obtained by magnetic sorting with the **Fe@MWCNTs** derivatives.

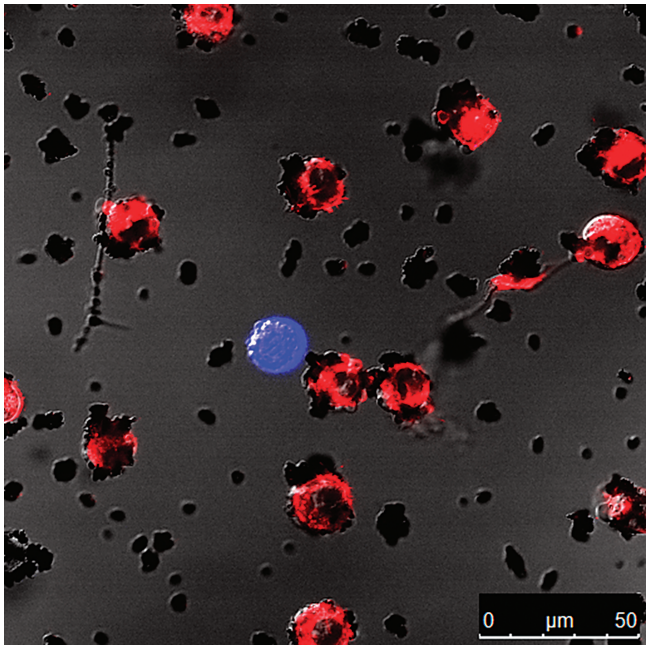

Figure 6. Exert of a zoomed confocal microscopy image of a cell mixture in the magnetically induced precipitate. One can clearly see that **Fe@MWCNTs-NHCO-Ab** nanomaterial selectively surrounds only EGFR+ A431 cells.

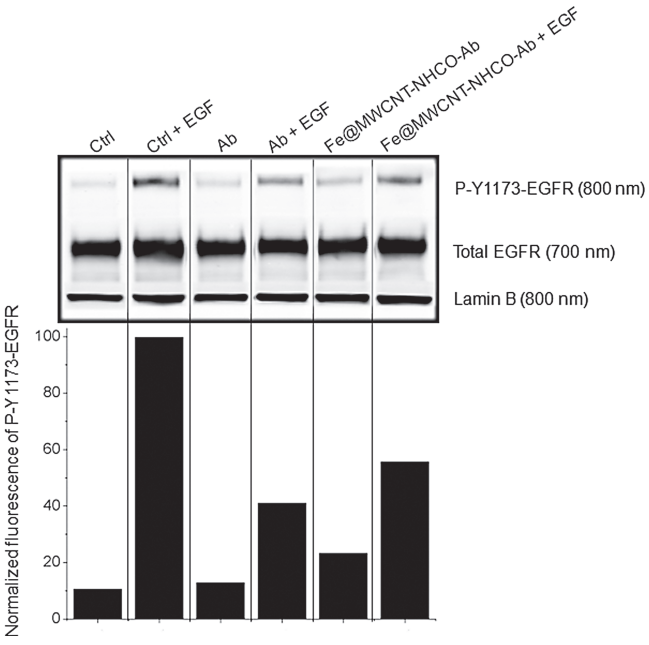

Figure 7. Western blot results after EGF-induced phosphorylation of the EGFR in A431 cells. EGF stimulation was performed with a concentration of 10 ng mL^{-1} (about 0.07 pmol, columns 2, 4, and 6) while equivalents mAb quantities of 5 µg mL^{-1} (about 33 pmol) alone (columns 3 and 4) or in **Fe@MWCNTs-NHCO-Ab** (columns 5 and 6) have been used, respectively.

Figure S15). This may be explained by the heterogeneous Fe-confinement of the initial **Fe@MWCNTs** precursors, as displayed by the TEM analysis. Furthermore, it is intuitive to consider that agglomerates of the magnetic particles, as in the case of **Fe@MWCNTs-NHCO-Ab** bounded to the cancer cells, move faster toward the magnetic pole following to generated field gradient if compared to the isolated particles (e.g., individual **Fe@MWCNTs-NHCO-Ab**),[18] due to the local accumulation of Fe. Zoomed confocal microscopy images, acquired immediately after the magnetic sorting experiments, clearly display that **Fe@MWCNTs-NHCO-Ab** selectively surrounds EGFR+ A431 cells only (**Figure 6** and Supporting Information Figure S16), imparting them sufficient magnetization for their abstraction, leaving unaffected EGFR- EAhy926 and CHO cells. In particular, 3D reconstructions of the cells suspension in the presence of **Fe@MWCNTs-NHCO-Ab**, obtained by recording the fluorescence intensities for several confocal planes, effectively shows that the magnetic nanotubes adhere at the exterior of the A431 cells membrane (Supporting Information Videos 1 and 2).

Aiming at detecting the biochemical consequences of the CNTs binding on EGFR+ A431 cells, phosphorylation studies and western blot analysis were undertaken. Upon induction of the EGFR phosphorylation at the Y1173 aminoacidic residue, through a short exposure of A431 cells to the epidermal growth factor (EGF), it was possible by western blot analysis to assess the increase in the signal of the phospho-EGFR, if compared with the basal level observed in the non-stimulated cells (**Figure 7**, column 1). As expected, the mAb was able to reduce the phosphorylation level by about 60% (Figure 7, column 4), while **Fe@MWCNTs-NHCO-Ab** showed a lower, but still remarkable, 50% decrease in EGF-induced phosphorylation of the EGFR (Figure 7, column 6). Beside the occurrence of the binding of **Fe@MWCNTs-NHCO-Ab**, as also revealed by ELISA, these findings suggest the inhibition of the biochemical action of the EGF stimulation. This means that in **Fe@MWCNTs-NHCO-Ab** conjugates, *Cetuximab*'s intrinsic ability to block the signal transduction pathways, causing cancer progression upon EGF overstimulation, is also preserved.[55]

2.4. Cytotoxicity Evaluation

As outlined in the previous session, the overall magnetic filtration experiment lasts for 10.5 min (2.5 for binding and 8 for the cell separation), and therefore the contact time between the cells and the nanotubes is very short, in particular for the EGFR- CHO and EAhy926 cell lines. As a way to assess the biocompatibility profile of **Fe@MWCNTs-NHCO-Ab** toward the chosen cell lines, we performed standard cytotoxicity assay through mitochondrial activity (formazan conversion, MTS). Dose-dependent cell viability results of the MTS assays after one-hour exposition of **Fe@MWCNTs-NHCO-Ab** and reference compounds on the EGFR- cell lines are plotted in **Figure 8** and listed in Supporting Table S3 (results on A431 cells are plotted in Supporting Information Figure S17). The cell viability percentages of CHO cells are clearly dose-dependent, resulting to be ca. 83%, 92% and 103% for the 200, 100, and 50 µg mL^{-1} solutions, respectively. Clearly, a minor decrease in cell viability was determined at the concentration used for the magnetic filtration experiments, even if the exposition time was six times

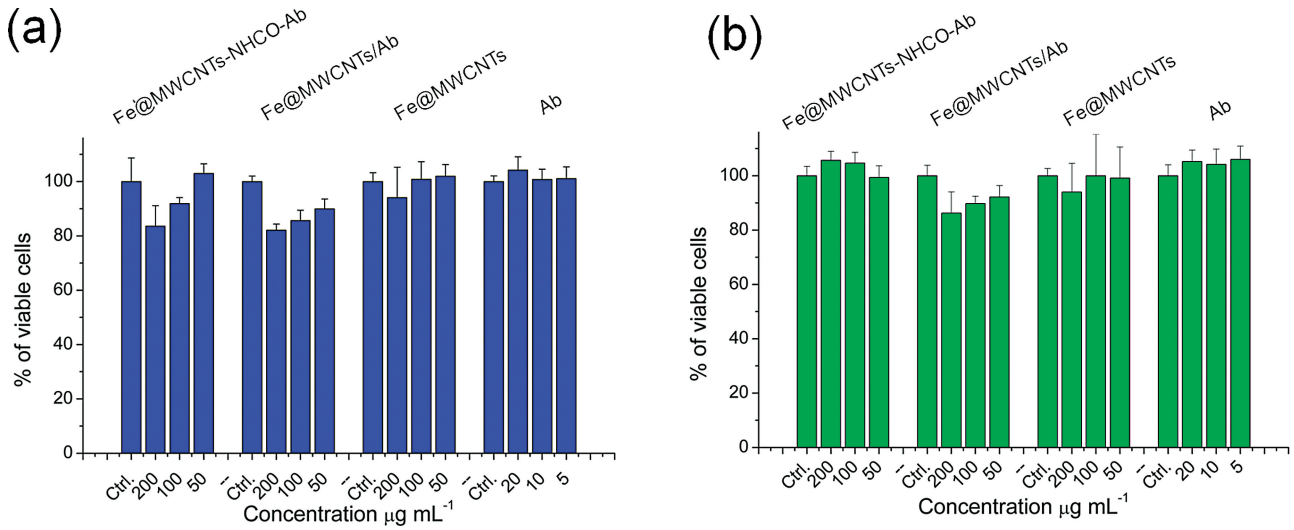

Figure 8. Cell viability percentages of a) CHO and b) EAhy926 cells as obtained by MTS assay after 1 h of exposition of equivalent amounts of **Fe@MWCNTs** (dosages of about 200, 100 and 50 μg mL^{-1}) and mAb (histograms of dosages of 20, 10 and 5 μg mL^{-1}). Results are expressed in percentages of viable cells and presented as means ± S.D. (n = 4).

higher than that required for the cell sorting experiments. The biocompatibility of **Fe@MWCNTs-NHCO-Ab** toward EAhy926 cells is even higher, with a steady percentage of cell viability around 100%. **Fe@MWCNTs/Ab** and **Fe@MWCNTs** showed respectively slightly higher and slightly lower reduction in cell viability of both cell lines if compared to **Fe@MWCNTs-NHCO-Ab**. However, considering the experimental errors and the sensitivity of the technique, it is difficult to draw any statistically significant conclusions. All together, these results indicate that the different compounds are well tolerated by the chosen cell lines. For the EGFR+ A431 cells, the viability after exposition to the different compounds revealed to be between 92% and 100% (97% with **Fe@MWCNTs-NHCO-Ab** at 100 μg mL^{-1}), again demonstrating the overall very low cytotoxicity of the **Fe@MWCNTs** derivatives.

2.5. Magnetic Fluid Hyperthermia (MFH) Experiments

Proof-of-principle stimuli-induced selective cytotoxicity on EGFR+ cells, via magnetic fluid hyperthermia (revealed by cell staining) have been undertaken. At first, at least three 0.28 cm^2 spots were imaged through optical microscopy imaging after trypan blue staining for each condition (Supporting Information Figure S18) allowing for both cumulative and statistical count (300–400 cells for each condition) of dead cells percentages (**Figure 9**), allowing to compare the extent (cumulative Figure 9a) and homogeneity in the distribution (statistical, Figure 9b) of cell mortality for each sample. As a preliminary test, electromagnetic radiation (frequency = 220 kHz, magnetic field strength = 83 kA m^{-1}) for 10 min of water-thermostated (37 °C) individual suspensions of A431 or EAhy926 cells did not caused noticeable cell death (cumulative 1.3% and 1.2%, statistical 1.2% ± 0.7% and 1.7% ± 1.5% for A431 and EAhy926, respectively). The administration of **Fe@MWCNTs-NHCO-Ab** (**Fe@MWCNTs** equivalent concentration of 200 μg mL^{-1}) induced a significant increase in cell death especially towards A431 cells (cumulative 11.7%, statistical 9.8% ± 4.1%) compared to EAhy926 (3.4%, and 3.3% ± 1.1%), with a very similar trend of that observed during the MTS assays (a "shift" of only 3–5% between these two viability assessment modalities has been detected). Very interestingly, upon administration of

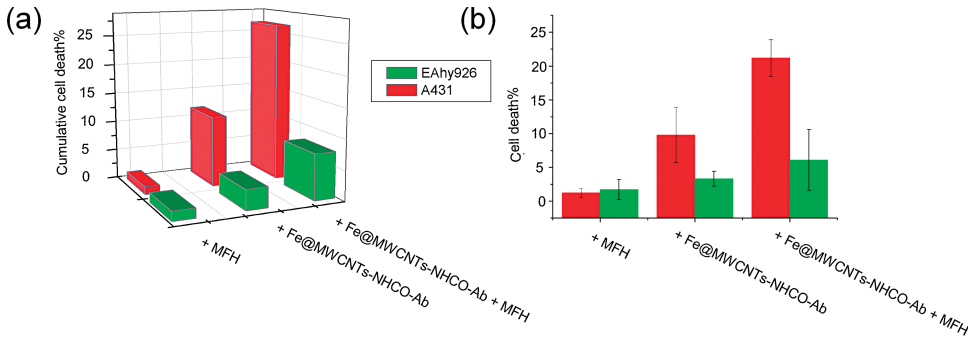

Figure 9. a) Cumulative and b) statistical count of cell dead percentages during the MFH induction and the control experiments.

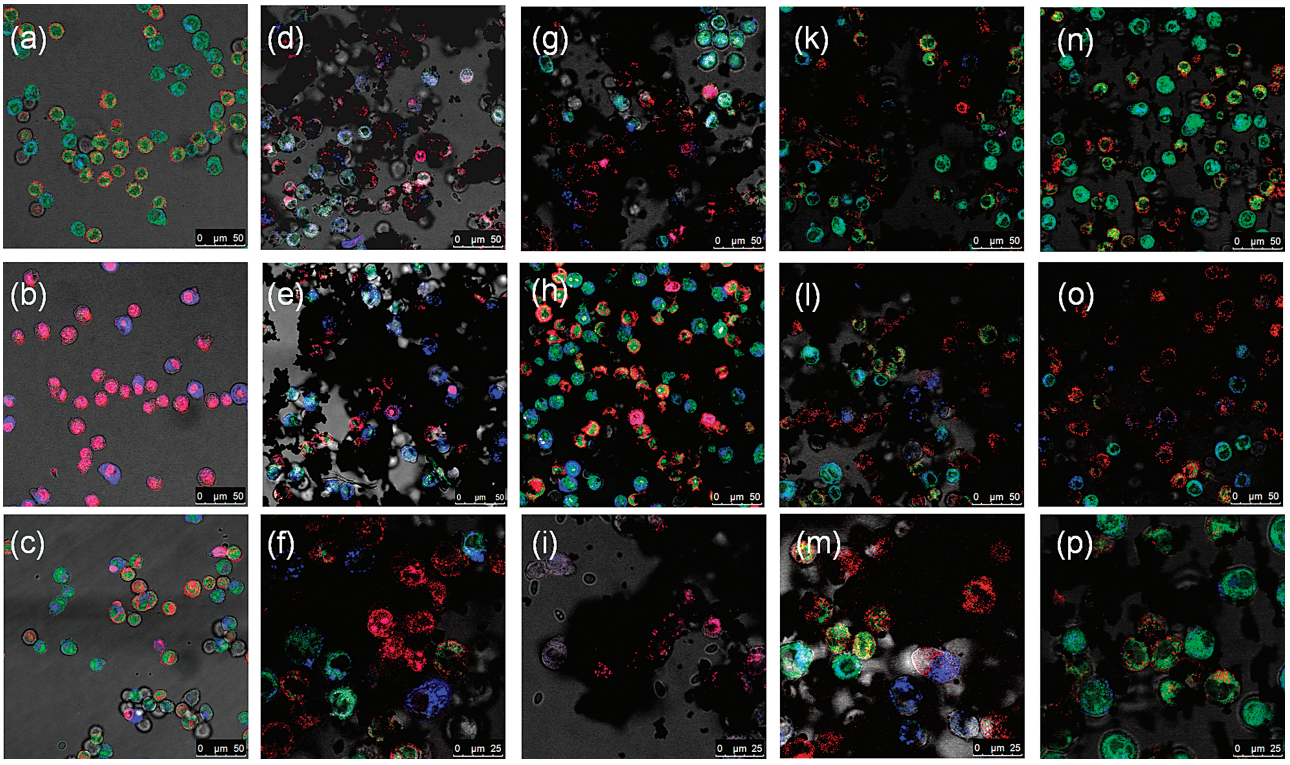

Figure 10. Confocal microscopy images after staining with ethidium bromide and acridine orange of mixtures containing A431 cells (red) and Eahy926 cells (blue) a) without any magnetic treatment, b) after 10 min at 70 °C, c) after 20 min of ultrasonication, d–i) after addition of **Fe@MWCNTs-NHCO-Ab** and exposure to the electromagnetic irradiation, and k–p) after exposure with only **Fe@MWCNTs-NHCO-Ab** alone in the absence of any irradiation.

Fe@MWCNTs-NHCO-Ab and concomitant MFH treatment, the induced cell mortality significantly rises for A431 cells (cumulative 26.7%, statistical 21.2% ± 2.7%), while only slightly increases are noticeable for EAhy926 cells (cumulative 7.7%, statistical 6.1% ± 4.5%). Under these conditions, the lack of quantitative suppression of the A431 cells (about 25%) is probably a consequence of the inhomogeneous distribution of the Fe inside the CNTs and of the moderate degree of Fe filling (about 7% w/w).

To shed further light on the selectivity of the observed magnetically-induced cytotoxicity toward cancer cells, we stained A431 (red) and EAhy926 cells (blue), and mixed them in the presence of Ethidium bromide/acridine orange staining chromophores, the latter being a known stainer for both dead and alive cells, respectively. In the absence of CNTs and magnetic field, the cells displayed blue or red tint and a background green coloration (acridine orange), indicating that they are viable (**Figure 10**a). On the other hand, if the same cell mixture is exposed to heat (70 °C, 10 min), cell death occurred and ethidium bromide staining takes place, turning the color of dead A431 and EAhy926 cells into magenta and blue-magenta, respectively (Figure 10b). A mixture of dead and alive A431 and EAhy926 cells is shown in Figure 10c as a reference. With the aim of maximizing the selective action of **Fe@MWCNTs-NHCO-Ab** toward A431 cells, the MFH treatment was exerted on the entangled CNT-cells precipitates as obtained *via* the magnetic filtration procedure (see above). In these conditions, the aforementioned MFH treatment was then applied (Figure 10d–i) and compared with the reference sample (in the presence of **Fe@MWCNTs-NHCO-Ab** but in absence of the electromagnetic radiation, Figure 10k–p). It can be clearly seen that fully magenta cells (dead A431 cells) are mainly detected in the MFH-treated samples, where **Fe@MWCNTs-NHCO-Ab** nanoconjugates efficiently surround EGFR+ A431 cells (Figure 10g,i, Supporting Information Videos 3 and 4). Without exposure to electromagnetic radiation, no elevated cytotoxicity was observed (Figure 10k,o,p, Supporting Information Video 5), in agreement with the cell viability found after trypan staining. Notably, in all of the experiments very rarely a dead EAhy926 cell was observed. As expected, control experiments conducted in the presence of the electromagnetic radiation only, did not induce any relevant cytotoxicity (Supporting Information Figure S19). Taken all together, these data clearly show how the presence of the targeting mAb units constitutes an essential prerequisite for reaching lethal local concentrations enhancing the residence time of the CNTs-based materials on the cancer cells.

2.6. Computational Studies

The goal of this computational part is to help at understanding how the mAb and the CNT macromolecules can interface with each other, as this could significantly influence the structural and conformational properties of the mAb counterpart and

thus, that of the two antigen binding regions, namely the Fabs. However, it should be pointed out that due to the high density and heterogeneous allocation of the NH_2 groups on the exosurface of **Fe@MWCNTs-NH$_2$** together with the homogeneous distribution of free carboxylic functionalities on to the antibody surface, it is virtually impossible to forecast a realistic model describing the covalent structure of **Fe@MWCNTs-NHCO-Ab**. In fact, by mapping the distribution of mAb's carboxylic acid groups (taken by the crystal structure of *Cetuximab* as solved by Harris et al.),[56] one can observe a uniform distribution of 124 amino acid residues (60 aspartates, 60 glutamates, 2 C-terminal cysteines and 2 C-terminal arginines), of which a restricted number (ca. 40%) is buried in the mAb's tertiary structure, shielded by other side chains. The other carboxylic acid residues, roughly 60%, are homogenously distributed on the outer antibody surface, all being potentially reactive toward amidation reactions with any of the terminal NH_2 groups exohedrally exposed on the functionalized CNT (Supporting Information Figure S20). Therefore, a prediction about the exact covalent structure of the CNT-mAb hybrid is very difficult and any attempts to suggest a representative structure are pure speculative. Nevertheless, experimental evidences (see above) have shown that the mAb easily adsorbs on **Fe@MWCNTs** upon simple mixing in aqueous solutions (already after a 2 min), thus suggesting a strong non-covalent affinity between the two macromolecular counterparts. Thus, among the different envisaged reaction pathways, it is realistic to think that the mAb macromolecules firstly adsorb onto the CNT surface and then undergoes covalent grafting through amidation reaction between the mAb's carboxylic acids and the neighboring NH_2 groups present on the CNT surface. Therefore, we have focused our attention on the modeling of the non-covalent **Fe@MWCNTs/mAb** complex. All-atom classical MD simulations have been firstly performed on the mAb alone to relax the structures before the docking calculations. For the mAb alone, its intrinsic flexibility was reflected by the 17 ns MD trajectory, showing a calculated RMSD of the protein backbone not converging to a stable value. Being the mAb structure constituted by three functional regions, two Fabs and one Fragment

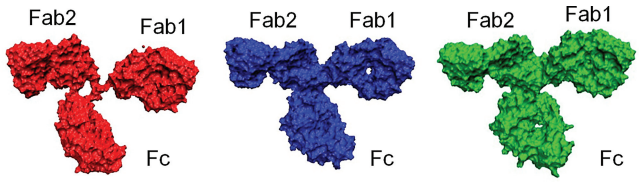

Figure 11. The three most representative *Cetuximab*'s conformations as obtained from the cluster analysis of 17 ns MD trajectory distinguished by coloration.

cristallizable (Fc) connected by highly-flexible hinge region, intense conformational fluctuations were observed during the MD simulations. On the other hand, when calculating the RMSD on the separate Fab1, Fab2, and Fc regions, a constant trend was observed, thus suggesting a fairly stability of the isolated fragments over the time (Supporting Information Figure S21). This confirms that the sampling done during the 17 ns MD simulation is sufficient to confidently carry on our computational studies. Considering the previous data, it is clear that the antibody structure cannot be efficiently represented by a single conformation. A cluster analysis was then performed, from which the three most representative conformations could be obtained (**Figure 11**). In all the conformations, the electrostatic potential mapping of the mAb's nicely displays a rather uniform surface polarity (Supporting Information Figure S22), thus clearly indicating the absence of a particular hydrophobic pocket that might drive, at a first glance, a preferential interaction with a CNT.

Therefore, to predict the interaction mode between the CNT exosurface and the mAb, we performed docking simulations of a 3D model of CNT (for computational efficiency reasons and considering a negligible effect of the inner layer, we have approximated our MWCNTs to a SWCNT with a 20 Å in diameter and 100 Å in length, labeled as CNT20) onto the three most representative conformations of *Cetuximab* as calculated above. As clearly observed in **Figure 12**, independently on the initial conformation of the mAb, the docking simulations generated the same distribution of the binding positions. Specifically, the

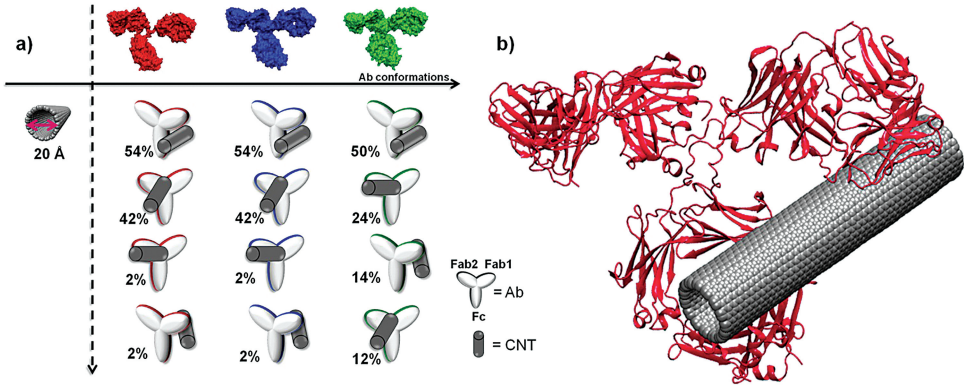

Figure 12. a) The interaction modes, predicted by docking calculations between CNT20 and the three mAb conformations, are sketched as cartoons and colored according to the conformations as displayed in Figure 11. The 50 adsorption modes as returned from each docking simulation runs are ranked, from the top to the bottom, in 4 main clusters, from the most to the lowest populated. b) Graphical representation of CNT-Ab complex (colored in grey and magenta, respectively) as the most recurred interaction mode.

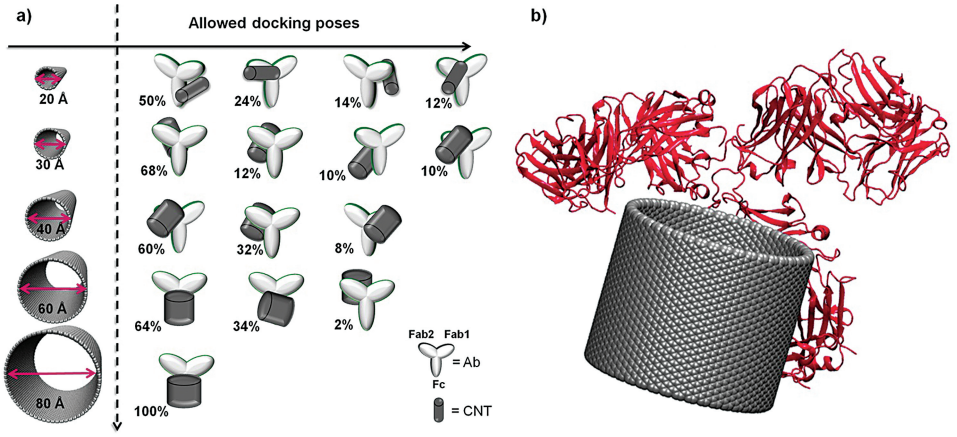

Figure 13. a) CNT-mAb adsorption modes as a function of the CNT's diameter docked onto the equilibrated structure of the antibody. Column: occupancy for each CNT-mAb adsorption mode as a function of the CNT's diameter. Row: occupancy for each CNT-mAb adsorption mode, ranked from the most to the lowest populated structure. b) The unique CNT-mAb conformation predicted for CNT80.

most populated docked adsorption mode (≥50% occupancy), recurring in all the simulations for CNT20, develops the CNT framework nested in the cavity between the Fab1 and Fc regions (i.e., Fab-Fc cavity), in which hydrophobic interactions are maximized (Figure 12). This adsorption mode obviously depends on the CNT's diameter, suggesting that its dimension plays a critical role in determining, among the most likely positions, the final structure. This means that such prediction is diameter-dependent and not significantly representative of the supramolecular interactions between all class of CNTs and the mAb. Consequently, a systematic docking analysis with CNTs of increasing diameters (d_{CNTs} = 30, 40, 60, and 80 Å, labeled as CNT30, CNT40, CNT60, and CNT80, respectively) was carried out on the *Cetuximab* equilibrated geometry (**Figure 13**).

From this systematic analysis, it clearly emerges that, increasing the CNTs' diameter, the predicted interaction modes for the small-diameter CNTs converge to a unique cluster in which the CNTs move away from the Fab-Fc cavity. In fact, CNTs featuring $d_{CNTs} \geq 80$ Å interact with the mAb only through the Fc region, leaving unaltered the Fabs regions (Figure 13a,b). Notably, in any of the discussed cases, the presence of the CNT structure does seem to sterically affect the conformational or chemical properties of the Fabs, thus further supporting the experimental biochemical findings for which the *Cetuximab*'s binding properties are largely preserved in the CNT-mAb hybrids.

3. Conclusions

In this work, we have shown that MWCNTs are very suitable scaffolds to cavity confine magnetic metallic species and orthogonally immobilize targeting antibodies on the external portion of the carbonaceous framework. The resulting bioactive nanomagnets showed a very good binding selectivity toward EGFR+ cancer cells inhibiting the biochemical actions triggered by the EGF stimulation of the EGFR. Moreover, it has been shown that these nanomagnets can be used for cell-sorting experiments, displaying a fast (few min!!) isolation of the EGFR+ cancers cells from the EGFR- cell lines. The cytotoxicity profiles as evaluated through mitochondrial cell viability studies showed a good biocompatibility behavior of the tested compounds. With the help of molecular dynamic and docking simulations, it has also been shown for the first time that the presence of the CNT framework does not sterically affect the conformational or chemical properties of the two antigen binding regions, thus further supporting the experimental biochemical findings for which the CNT-mAb hybrids largely retain the binding properties of *Cetuximab* alone. Proof-of-principle MFH experiments showed remarkable selectivity toward the killing of cancer cells (EGFR+ >> EGFR-) and a two-fold increase for the suppression of cancer cells. However, the moderate overall killing efficiency (ca. 25%) suggest that an improvement of the structural properties of the CNTs in terms of both Fe content and homogeneity of Fe distribution in the CNTs is necessary to engineer a full operative theranostic tool. These two parameters are currently under optimization in our laboratory by developing new CVD protocols. In perspective, the possibility of virtually attaching any bioactive molecule and increasing the Fe filling to ameliorate MFH responses make such Fe@MWCNTs exceptional multifunctional scaffolds that, if properly functionalized, would open the way to a brand new class of nanomedical tools potentially displaying an unnumbered combination of theranostic actions. All these research activities represent the next exciting challenges that we are undertaking in our future research endeavors in this field.

Supporting Information

Supporting Information is available from the Wiley Online Library or from the author.

Acknowledgements

D.B. thanks generous support by EU (ITN "FINELUMEN" PITN-GA-2008-215399), the FRS-FNRS, (FRFC contracts no. 2.4.550.09 and 2.4.617.07.F and MIS no. F.4.505.10. F), the "Loterie Nationale", the Région Wallonne

through the "TARGAN" project, the "TINTIN" ARC project (09/14-023) and the University of Namur (internal funding). Access to the computational resources supplied by CASPUR HPC Grant 2011 on GPU cluster, the CINECA, and by the TARTAGLIA cluster at the University of Trieste. R.M. thanks FRS-FNRS for his post-doctoral fellowship. F.P. thanks FRS-FNRS for his FRIA doctoral fellowship. Y.G. thanks funding support by IAP INANOMAT, FNRS (FRFC 2.4508.08, IISN 4.4507.10). The authors thank Noelle Ninane and Catherine Demazy for the observations in confocal microscopy, Edith Roegiers and Marie Genin for the advices during western blot preparation and Dr. Chiara Fabbro for the Raman and TGA under air measurements. Detailed experimental procedures and setup, ^{57}Fe Mossbauer parameters, AFM, TEM and SEM analysis, Raman spectroscopy, EDS, XPS, TGA and XRD results, gel electrophoresis, and confocal microscopy characterizations of the magnetic filtration steps, optical microscope images after trypan blue staining and confocal microscopy images after EtBr/acridine orange staining following MFH, computational predictive structures and analysis.

Received: October 5, 2012
Revised: December 16, 2012
Published online: January 29, 2013

[1] http://globocan.iarc.fr/(accessed January 2013).
[2] a) S. Iijima, *Nature* **1991**, *354*, 56; b) S. Iijima, T. Ichihashi, *Nature* **1993**, *363*, 603.
[3] a) H. Hong, T. Gao, W. Cai, *Nano Today* **2009**, *4*, 252; b) K. T. Al-Jamal, H. Nerl, K. H. Müller, H. Ali-Boucetta, S. Li, P. D. Haynes, J. R. Jinschek, M. Prato, A. Bianco, K. Kostarelos, A. E. Porter, *Nanoscale* **2011**, *3*, 2627.
[4] S. L. Edwards, J. A. Werkmeister, J. A. M. Ramshaw, *Expert Rev. Med. Dev.* **2009**, *6*, 499.
[5] a) G. Pastorin, W. Wu, S. Wieckowski, J. P. Briand, K. Kostarelos, M. Prato, A. Bianco, *Chem. Commun.* **2006**, 1182; b) S. K. Vashist, D. Zheng, G. Pastorin, K. Al-Rubeaan, J. H. T. Luong, F. S. Sheu, *Carbon* **2011**, *49*, 4077; c) W. Wu, S. Wieckowski, G. Pastorin, M. Benincasa, C. Klumpp, J. P. Briand, R. Gennaro, M. Prato, A. Bianco, *Angew. Chem. Int. Ed.* **2005**, *44*, 6358; d) C. Menard-Moyon, E. Venturelli, C. Fabbro, C. Samori, T. Da Ros, K. Kostarelos, M. Prato, A. Bianco, *Expert Opin. Drug Discovery* **2010**, *5*, 691.
[6] a) C. Samorì, H. Ali-Boucetta, R. Sainz, C. Guo, F. M. Toma, C. Fabbro, T. Da Ros, M. Prato, K. Kostarelos, A. Bianco, *Chem. Commun.* **2010**, *46*, 1494; b) C. Gaillard, G. Cellot, S. Li, F. M. Toma, H. Dumortier, G. Spalluto, B. Cacciari, M. Prato, L. Ballerini, A. Bianco, *Adv. Mater.* **2009**, *21*, 2903; c) S. R. Ji, C. Liu, B. Zhang, F. Yang, J. Xu, J. A. Long, C. Jin, D. L. Fu, Q. X. Ni, X. J. Yu, *Biochim. Biophys. Acta Rev. Cancer* **2010**, *1806*, 29.
[7] a) K. Kostarelos, L. Lacerda, G. Pastorin, W. Wu, S. Wieckowski, J. Luangsivilay, S. Godefroy, D. Pantarotto, J. P. Briand, S. Muller, M. Prato, A. Bianco, *Nat. Nanotechnol.* **2007**, *2*, 108; b) A. Bianco, K. Kostarelos, M. Prato, *Chem. Commun.* **2011**, *47*, 10182; c) K. Kostarelos, A. Bianco, M. Prato, *Nat. Nanotechnol.* **2009**, *4*, 627; d) H. K. Moon, S. H. Lee, H. C. Choi, *ACS Nano* **2009**, *3*, 3707; e) D. Shi, Y. Guo, Z. Dong, J. Lian, W. Wang, G. Liu, L. Wang, R. C. Ewing, *Adv. Mater.* **2007**, *19*, 4033; f) L. Lacerda, A. Bianco, M. Prato, K. Kostarelos, *J. Mater. Chem.* **2008**, *18*, 17; g) A. Al Faraj, K. Cieslar, G. Lacroix, S. Gaillard, E. Canet-Soulas, Y. Crémillieux, *Nano Lett.* **2009**, *9*, 1023; h) Z. Liu, S. Tabakman, K. Welsher, H. Dai, *Nano Res.* **2009**, *2*, 85; i) S. Y. Hong, G. Tobias, K. T. Al-Jamal, B. Ballesteros, H. Ali-Boucetta, S. Lozano-Perez, P. D. Nellist, R. B. Sim, C. Finucane, S. J. Mather, M. L. H. Green, K. Kostarelos, B. G. Davis, *Nat. Mater.* **2010**, *9*, 485; j) Z. Liu, W. Cai, L. He, N. Nakayama, K. Chen, X. Sun, X. Chen, H. Dai, *Nat. Nanotechnol.* **2007**, *2*, 47; k) S. T. Yang, K. A. S. Fernando, J. H. Liu, J. Wang, H. F. Sun, Y. Liu, M. Chen, Y. Huang, X. Wang, H. Wang, Y. P. Sun, *Small* **2008**, *4*, 940.
[8] A. A. Bhirde, V. Patel, J. Gavard, G. Zhang, A. A. Sousa, A. Masedunskas, R. D. Leapman, R. Weigert, J. S. Gutkind, J. F. Rusling, *ACS Nano* **2009**, *3*, 307.
[9] X. Ding, R. Singh, A. Burke, H. Hatcher, J. Olson, R. A. Kraft, M. Schmid, D. Carroll, J. D. Bourland, S. Akman, F. M. Torti, S. V. Torti, *Nanomedicine* **2011**, *6*, 1341.
[10] C. J. Gannon, P. Cherukuri, B. I. Yakobson, L. Cognet, J. S. Kanzius, C. Kittrell, R. B. Weisman, M. Pasquali, H. K. Schmidt, R. E. Smalley, S. A. Curley, *Cancer* **2007**, *110*, 2654.
[11] a) C. W. Lam, J. T. James, R. McCluskey, R. L. Hunter, *Toxicol. Sci.* **2004**, *77*, 126; b) M. L. Schipper, N. Nakayama-Ratchford, C. R. Davis, N. W. S. Kam, P. Chu, Z. Liu, X. Sun, H. Dai, S. S. Gambhir, *Nat. Nanotechnol.* **2008**, *3*, 216.
[12] D. Tasis, N. Tagmatarchis, A. Bianco, M. Prato, *Chem. Rev.* **2006**, *106*, 1105.
[13] Y. Gao, I. Kyratzis, *Bioconjugate Chem.* **2008**, *19*, 1945.
[14] H. Dumortier, S. Lacotte, G. Pastorin, R. Marega, W. Wu, D. Bonifazi, J. P. Briand, M. Prato, S. Muller, A. Bianco, *Nano Lett.* **2006**, *6*, 1522.
[15] L. Lacerda, M. A. Herrero, K. Venner, A. Bianco, M. Prato, K. Kostarelos, *Small* **2008**, *4*, 1130.
[16] M. A. Herrero, L. Lacerda, A. Bianco, K. Kostarelos, M. Prato, *Int. J. Nanotechnol.* **2011**, *8*, 885.
[17] a) A. N. Khlobystov, D. A. Britz, G. A. D. Briggs, *Acc. Chem. Res.* **2005**, *38*, 901; b) M. Yudasaka, K. Ajima, K. Suenaga, T. Ichihashi, A. Hashimoto, S. Iijima, *Chem. Phys. Lett.* **2003**, *380*, 42; c) F. Simon, H. Kuzmany, H. Rauf, T. Pichler, J. Bernardi, H. Peterlik, L. Korecz, F. Fülöp, A. Jánossy, *Chem. Phys. Lett.* **2004**, *383*, 362.
[18] I. K. Herrmann, R. N. Grass, W. J. Stark, *Nanomedicine* **2009**, *4*, 787.
[19] T. W. Chamberlain, A. Camenisch, N. R. Champness, G. A. D. Briggs, S. C. Benjamin, A. Ardavan, A. N. Khlobystov, *J. Am. Chem. Soc.* **2007**, *129*, 8609.
[20] T. Takenobu, T. Takano, M. Shiraishi, Y. Murakami, M. Ata, H. Kataura, Y. Achiba, Y. Iwasa, *Nat. Mater.* **2003**, *2*, 683.
[21] L. Jankovič, D. Gournis, P. N. Trikalitis, I. Arfaoui, T. Cren, P. Rudolf, M.-H. Sage, T. T. M. Palstra, B. Kooi, J. De Hosson, M. A. Karakassides, K. Dimos, A. Moukarika, T. Bakas, *Nano Lett.* **2006**, *6*, 1131.
[22] a) G. A. Rance, D. H. Marsh, S. J. Bourne, T. J. Reade, A. N. Khlobystov, *ACS Nano* **2010**, *4*, 4920; b) A. La Torre, G. A. Rance, J. El Harfi, J. Li, D. J. Irvine, P. D. Brown, A. N. Khlobystov, *Nanoscale* **2010**, *2*, 1006; c) M. Del Carmen Giménez-López, F. Moro, A. La Torre, C. J. Gómez-García, P. D. Brown, J. Van Slageren, A. N. Khlobystov, *Nat. Commun.* **2011**, *2*, 407.
[23] C. Xu, J. Sloan, G. Brown, S. Bailey, V. C. Williams, S. Friedrichs, K. S. Coleman, E. Flahaut, J. L. Hutchison, R. E. Dunin-Borkowski, M. L. H. Green, *Chem. Commun.* **2000**, 2427.
[24] C. Guerret-Piecourt, Y. L. Bouar, A. Lolseau, H. Pascard, *Nature* **1994**, *372*, 761.
[25] a) J. Li, S. Q. Yap, S. L. Yoong, T. R. Nayak, G. W. Chandra, W. H. Ang, T. Panczyk, S. Ramaprabhu, S. K. Vashist, F. S. Sheu, A. Tan, G. Pastorin, *Carbon* **2012**, *50*, 1625; b) Y. Ren, G. Pastorin, *Adv. Mater.* **2008**, *20*, 2031.
[26] P. Singh, S. Campidelli, S. Giordani, D. Bonifazi, A. Bianco, M. Prato, *Chem. Soc. Rev.* **2009**, *38*, 2214.
[27] E. Roduner, *Chem. Soc. Rev.* **2006**, *35*, 583.
[28] a) A. H. Lu, E. L. Salabas, F. Schuth, *Angew. Chem. Int. Ed.* **2007**, *46*, 1222; b) H. Zeng, S. Sun, *Adv. Funct. Mater.* **2008**, *18*, 391; c) Y. W. Jun, J. S. Choi, J. Cheon, *Chem. Commun.* **2007**, 1203.
[29] a) V. I. Shubayev, T. R. Pisanic Ii, S. Jin, *Adv. Drug Delivery Rev.* **2009**, *61*, 467; b) A. Ito, M. Shinkai, H. Honda, T. Kobayashi, *J. Biosci. Bioeng.* **2005**, *100*, 1; c) Q. A. Pankhurst, J. Connolly, S. K. Jones, J. Dobson, *J. Phys. D* **2003**, *36*, R167; d) A. K. Gupta, R. R. Naregalkar, V. D. Vaidya, M. Gupta, *Nanomedicine* **2007**, *2*, 23; e) E. Amstad,

M. Textor, E. Reimhult, *Nanoscale* **2011**, *3*, 2819; f) M. Mahmoudi, S. Sant, B. Wang, S. Laurent, T. Sen, *Adv. Drug Delivery Rev.* **2011**, *63*, 24; g) F. M. Kievit, M. Zhang, *Acc. Chem. Res.* **2011**, *44*, 853.

[30] a) H. Gu, K. Xu, C. Xu, B. Xu, *Chem. Commun.* **2006**, 941; b) J. Bao, W. Chen, T. Liu, Y. Zhu, P. Jin, L. Wang, J. Liu, Y. Wei, Y. Li, *ACS Nano* **2007**, *1*, 293; c) P. C. Lin, M. C. Tseng, A. K. Su, Y. J. Chen, C. C. Lin, *Anal. Chem.* **2007**, *79*, 3401; d) D. Horák, M. Babič, H. Macková, M. J. Beneš, *J. Separ. Sci.* **2007**, *30*, 1751; e) K. El-Boubbou, C. Gruden, X. Huang, *J. Am. Chem. Soc.* **2007**, *129*, 13392; f) I. S. Lee, N. Lee, J. Park, B. H. Kim, Y. W. Yi, T. Kim, T. K. Kim, I. H. Lee, S. R. Paik, T. Hyeon, *J. Am. Chem. Soc.* **2006**, *128*, 10658; g) R. Di Corato, N. C. Bigall, A. Ragusa, D. Dorfs, A. Genovese, R. Marotta, L. Manna, T. Pellegrino, *ACS Nano* **2011**, *5*, 1109; h) R. Di Corato, P. Piacenza, M. Musarò, R. Buonsanti, P. D. Cozzoli, M. Zambianchi, G. Barbarella, R. Cingolani, L. Manna, T. Pellegrino, *Macromol. Biosci.* **2009**, *9*, 952; i) X. Diao, H. Chen, G. Zhang, F. Zhang, X. Fan, *J. Nanomater.* **2012**, *2012*.

[31] a) O. Veiseh, J. W. Gunn, M. Zhang, *Adv. Drug Delivery Rev.* **2010**, *62*, 284; b) B. Polyak, G. Friedman, *Expert Opin. Drug Delivery* **2009**, *6*, 53; c) S. C. McBain, H. H. P. Yiu, J. Dobson, *Int. J. Nanomed.* **2008**, *3*, 169.

[32] a) C. Sun, J. S. H. Lee, M. Zhang, *Adv. Drug Delivery Rev.* **2008**, *60*, 1252; b) W. Chen, D. P. Cormode, Z. A. Fayad, W. J. M. Mulder, *Wiley Interdiscip. Rev. Nanomed. Nanobiotechnol.* **2011**, *3*, 146.

[33] a) C. S. S. R. Kumar, F. Mohammad, *Adv. Drug Delivery Rev.* **2011**, *63*, 789; b) T. Kobayashi, *Biotechnol. J.* **2011**, *6*, 1342; c) I. Sharifi, H. Shokrollahi, S. Amiri, *J. Magn. Magn. Mater.* **2012**, *324*, 903.

[34] F. Yang, C. Jin, D. Yang, Y. J. Jiang, J. Li, Y. Di, J. H. Hu, C. C. Wang, Q. X. Ni, D. L. Fu, *Eur. J. Cancer* **2011**, *47*, 1873.

[35] B. D. Chen, H. Zhang, C. X. Zhai, N. Du, C. Sun, J. W. Xue, D. R. Yang, H. Huang, B. Zhang, Q. P. Xie, Y. L. Wu, *J. Mater. Chem.* **2010**, *20*, 9895.

[36] M. Kumar, Y. Ando, *J. Nanosci. Nanotechnol.* **2010**, *10*, 3739.

[37] D. Cai, J. M. Mataraza, Z. H. Qin, Z. P. Huang, J. Y. Huang, T. C. Chiles, D. Carnahan, K. Kempa, Z. F. Ren, *Nat. Methods* **2005**, *2*, 449.

[38] O. Vittorio, P. Quaranta, V. Raffa, N. Funel, D. Campani, S. Pelliccioni, B. Longoni, F. Mosca, A. Pietrabissa, A. Cuschieri, *Nanomedicine* **2011**, *6*, 43.

[39] U. Weissker, S. Hampel, A. Leonhardt, B. Büchner, *Materials* **2010**, *3*, 4387.

[40] I. Monch, A. Meye, A. Leonhardt, K. Kramer, R. Kozhuharova, T. Gemming, M. P. Wirth, B. Buchner, *J. Magn. Magn. Mater.* **2005**, *290*, 276.

[41] A. Taylor, K. Lipert, K. Kramer, S. Hampel, S. Fussel, A. Meyel, R. Klingeler, M. Ritschel, A. Leonhardt, B. Buchner, M. P. Wirth, *J. Nanosci. Nanotechnol.* **2009**, *9*, 5709.

[42] E. C. Vermisoglou, G. Pilatos, G. E. Romanos, E. Devlin, N. K. Kanellopoulos, G. N. Karanikolos, *Nanotechnology* **2011**, *22*.

[43] F. Rivera, M. E. Vega-Villegas, M. F. Lopez-Brea, *Anti-Cancer Drugs* **2008**, *19*, 99.

[44] B. R. Voldborg, L. Damstrup, M. Spang-Thomsen, H. S. Poulsen, *Ann. Oncol.* **1997**, *8*, 1197.

[45] J. B. Johnston, S. Navaratnam, M. W. Pitz, J. M. Maniate, E. Wiechec, H. Baust, J. Gingerich, G. P. Skliris, L. C. Murphy, M. Los, *Curr. Med. Chem.* **2006**, *13*, 3483.

[46] J. Goldstein, D. E. Newbury, D. C. Joy, C. E. Lyman, P. Echlin, E. Lifshin, L. Sawyer, J. R. Michael, in *Scanning Electron Microscopy and X-ray Microanalysis* (Ed: J. Goldstein), Springer, New York, NY USA **2003**, Ch. 9.

[47] P. Van der Heide, in *X-ray Photoelectron Spectroscopy: An introduction to Principles and Practices* (Ed: P. Van der Heide), Wiley VCH, Hoboken, NJ, USA **2012**, Ch. 4.

[48] J. F. Marco, J. R. Gancedo, A. Hernando, P. Crespo, C. Prados, J. M. Gonzalez, N. Grobert, M. Terrones, D. R. M. Walton, H. W. Kroto, *Hyperfine Interact.* **2002**, *139*, 535.

[49] C. Prados, P. Crespo, J. M. Gonzalez, A. Hernando, J. F. Marco, R. Gancedo, N. Grobert, M. Terrones, R. M. Walton, H. W. Kroto, *Phys. Rev. B* **2002**, *65*.

[50] B. David, N. Pizurova, O. Schneeweiss, V. Kudrle, O. Jasek, P. Synek, *Jpn. J. Appl. Phys.* **2011**, *50*.

[51] A. Khasanov, J. He, J. Gaillard, K. Yang, A. M. Rao, C. M. Cameron, J. M. Schmeltzer, J. G. Stevens, A. Nath, *Appl. Phys. Lett.* **2008**, *93*.

[52] a) J. L. Bahr, J. M. Tour, *Chem. Mater.* **2001**, *13*, 3823; b) M. Quintana, H. Traboulsi, A. Llanes-Pallas, R. Marega, D. Bonifazi, M. Prato, *ACS Nano* **2011**, *6*, 23.

[53] N. Tagmatarchis, M. Prato, *J. Mater. Chem.* **2004**, *14*, 437.

[54] E. Venturelli, C. Fabbro, O. Chaloin, C. Menard-Moyon, C. R. Smulski, T. Da Ros, K. Kostarelos, M. Prato, A. Bianco, *Small* **2011**, *7*, 2179.

[55] J. Graham, M. Muhsin, P. Kirkpatrick, *Nat. Rev. Drug Discovery* **2004**, *3*, 549.

[56] L. J. Harris, S. B. Larson, K. W. Hasel, A. McPherson, *Biochemistry* **1997**, *36*, 1581.